Nanoscale control of temperature operation ranges for magnetocaloric applications

Juan Sebastián Salcedo Gallo[1], Andreas Berger[2], Mikel Quintana[2], Elisabeth Restrepo Parra[1], Lorenzo Fallarino[2]

[1] Departamento de Física y Química, Universidad Nacional de Colombia, Manizales, Colombia

[2] CIC nanoGUNE BRTA, E-20018 Donostia-San Sebastián, Spain

Abstract

We devised a proof-of-concept materials design that addresses the necessary requirements for magnetocaloric materials to have a constant magnetocaloric effect over a large temperature range. For this purpose, we have fabricated epitaxial $Co_{1-x(z)}Ru_{x(z)}$ films engineered to have a triangular gradient in exchange strength J along the thickness. Different from homogeneous $Co_{1-x}Ru_x$ layers, where the maximum value of magnetic entropy change ΔS_m falls rapidly with temperature away from the ferromagnetic-paramagnetic phase transition, the $Co_{1-x(z)}Ru_{x(z)}$ graded structures exhibit high magnetocaloric effects over a large temperature range, leading to an improved cooling capacity. Theoretical modeling results confirm the enhanced temperature range and highlight a core aspect of our exchange graded materials approach, namely the ability to control and manipulate magnetism at nanoscale dimensions. As we demonstrate, this control is reliant on the fact that the temperature driven paramagnetic-ferromagnetic phase transition does not occur in the entirety of the material system but only in well-defined nanoscopic regions of our samples at any given temperature, enabling us to significantly extend the useful temperature range for magneto-caloric utilization.

1. Introduction

The magnetocaloric effect (MCE) was discovered almost a century ago [1,2], representing the isothermal entropy change or the adiabatic temperature change of a magnetic material upon the application or removal of an external magnetic field [3]. It has long been used for cryogenic operation to achieve millikelvin temperatures mostly employing paramagnetic salts, whose magnetic susceptibility diverges near T = 0 K [4]. The turning point towards broader practical implementations of MCE near room temperature (RT) was the demonstration of a regenerative thermodynamic cycle in gadolinium [5], a metal with a sizable MCE close to its Curie temperature $T_C \approx 293$ K [6]. Its subsequent implementation into a successful proof-of-principle cooling unit [7] has triggered substantial research activities resulting in the milestone observation of the giant MCE [8-14]. It was first reported in $Gd_5(Si_2Ge_2)$, a material that exhibits a first order structural transition immediately below its T_C [15],

which generates anomalously large peak values for the magnetic entropy change ΔS_m. However, the width of these peaks is very narrow, limiting the applicability of such materials for cyclic operations covering a practically relevant temperature range [16]. Additional problems include the hysteretic behavior associated with such first order phase transitions (FOPT), which results in wasted energy that could otherwise be used for refrigeration processes.

Another relevant parameter for evaluating the performance of MCE is the relative cooling power (RCP), which corresponds to the amount of heat that can be transferred between cold and hot reservoirs, usually calculated as the integral of the ΔS_m peak within its full temperature width at half maximum (FWHM) [18]. The RCP values for materials with a second order phase transitions (SOPT) can be far larger than those for FOPT systems and, due to their lack of thermal hysteresis, SOPT materials are now frequently used in magnetic refrigerator prototypes [18]. Nonetheless, for this technology to disrupt existing vapor compression commercial devices, researchers have yet to find improved pathways towards designing effective magnetocaloric materials and engineering efficient solid-state magnetic cooling systems [17]. Concerning Ericsson-type magnetic refrigerators, previous studies concluded that the ideal SOPT material should exhibit a constant ΔS_m value in the temperature range of the thermodynamic cycle operation [1,18,19]. In line with this, the scientific community is investing substantial efforts to develop a methodology to expand the temperature operation range of magnetic refrigerant devices and consequently the RCP through various methods [20], including structural amorphization [21,22], microalloying and annealing [23-25], nanostructuring [26-28], fabricating (nano-)composites [29-32], and employing multilayered materials [33-36]. All of them involve either the existence of a volume averaged T_C distribution in the magnetic material, or the presence of multiple successive magnetic phase transitions that contribute to broaden the ΔS_m curve and consequently enhance the RCP [37,38]. In this context, there is a great need to further expand the range of accessible RCP values and develop novel and improved ways to deterministically control it by adapting materials properties even better.

Pre-designed composition depth profiles could be employed in this context to tailor the magnetocaloric response of a material to realize major advances [39]. In fact, in exchange strength J graded magnetic system, a continuous set of quasi-SOPTs can be induced, whose characteristics can be controlled with both temperature and magnetic field [39,40]. It should be noted that although ferromagnetism is a long-range collective phenomenon, the local thermodynamic state of graded ferromagnets is dominated by the corresponding local material properties, down to distances of few nm [40]. At and above this length scale, such materials behave as they were composed of virtually independent (sub-)layers, each with their own "local" Curie temperature ($\tilde{T}_C$) [39,40]. However, from a fundamental thermodynamic perspective, such a system does not truly exhibit multiple phase transitions, but instead only one at a "global" Curie temperature (T_C). Such localization of

thermodynamic behavior leads to boundaries between strongly and weakly magnetized regions that can be controllably moved within the material upon changing the temperature or the magnetic field and therefore, it should be possible to utilize them to control and tailor RCP values as needed for a wide variety of materials.

To explore materials that have a pre-defined exchange strength J gradient along their thickness, we chose CoRu as a prototype because it forms isomorphous solid solutions, and its T_C changes almost linearly with composition [41]. By varying the Ru content during growth, a J profile (and thus a $\tilde{T}_C$ profile) can be achieved in films with depth (z) dependent compositions, e.g., $Co_{1-x(z)}Ru_{x(z)}$ [40]. The main motivation of the present work is to investigate whether and how such depth-dependent $\tilde{T}_C$ profiles can be utilized to modify the temperature extension of the paramagnetic (PM) – ferromagnetic (FM) phase transition, with particular emphasis on the RCP figure of merit for magnetocaloric materials. Our work here is attempting to contribute towards an overall understanding of thermal effects in suitably designed non uniform materials whose behavior is dominated by controlling ferromagnetic exchange coupling on the nanoscale and enabling a promising pathway towards achieving the so-called table-like MCE behavior [42]. Moreover, we performed Monte Carlo (MC) simulations to explore whether the experimentally observed behavior could be corroborated with this accurate type of calculation [43].

The paper is organized as follows: we describe in Sec. 2 all experimental and simulation methods. The material design and structural characterization are presented in Sec. 3 and the results of our magnetometry studies in Sec. 4. The magnetocaloric properties are discussed in Sec. 5, whereas in Sec. 6 we present our MC simulations results. In Sec. 7, we summarize our work, provide conclusions, and give an outlook.

2. Experimental and simulation details

All the epitaxial films were prepared by dc magnetron sputter and co-sputter deposition in an ultrahigh vacuum deposition system (ATC series from AJA International, Inc.) with a base pressure of better than 1.2×10^{-6} Pa. Hydrofluoric acid etched Si (110) were used as substrates. For each layer, the deposition process was started only after pre-sputtering each of the targets, using an Ar pressure of 0.4 Pa. The structural analysis was performed by means of x-ray diffraction (XRD) utilizing a PANalytical X'Pert Pro diffractometer with Cu-K_α radiation. Magnetization measurements were carried out using a commercial MicroMag 3900 vibrating sample magnetometer (VSM), equipped with a 360° rotational stage, allowing for an angular precision of better than 1° and a furnace capable of covering the temperature range 293 K ≤ T ≤ 1073 K with a temperature resolution of better than 1 K. During the furnace operation, the sample zone was continuously evacuated by an extraction pump and filled with a constant flow of helium gas while being covered by a radiation shield to reduce temperature gradients.

The simulations presented in this work were carried out using VEGAS [44], which is an open-source package for the atomistic simulation of magnetic materials, using the MC method based on the Metropolis algorithm. An adaptive spin update policy was used for an optimal phase space sampling of Heisenberg spin systems [44]. We have considered systems of $L = 20$ and $t = 60$, with L and t being the dimensions in the $x-y$ plane and along the z-axis, respectively [43]. Furthermore, it should be mentioned that the exchange coupling J is modulated along the z-axis, where $0 \leq z \leq t$ and therefore, t is defined in units of atomic layers (z). We obtain a system size of $N = L \times L \times t$, where we have executed $N \times N_{MCS}$ Monte Carlo Steps (MCS), with $N_{MCS} = 2 \times 10^4$, for every simulated temperature k_BT/J_{max} (with J_{max} being the largest exchange coupling strength within each simulated system), rejecting the first half of all MCS for relaxation. To compute statistical errors, we simulated five different initializations per configuration, for every temperature and every system explored in this work. We included periodic boundary conditions (PBC) in the $x-y$ plane to approach translational invariance within the plane of each layer, whereas free boundary conditions (FBC) were imposed along the z-axis to mimic the surface effects that occur on actual films.

3. Material design and structural characterization

For our experimental approach, it is most suitable to select a specific thin film material system that can be epitaxially fabricated with in-plane uniaxial magnetocrystalline anisotropy to have negligible demagnetizing effects. This ensures that our samples exhibit very simple magnetization reversal behavior, which is dominated by magnetization rotation and switching, and produces uniform magnetization states for nearly all external field strengths and orientations [40,45-48]. As a random alloy, CoRu adopts the hexagonal close packed crystal structure over a wide Ru dopant range and exhibits a magnetic easy axis (EA) behavior along its c-axis. Thus, we have utilized CoRu alloys for our films [45-48], whose layer structure is shown in Fig. 1(a). Ag and Cr underlayers were first deposited to promote highly oriented (211) $Cr_{0.804}Ru_{0.196}$ layers, which in turn served as a template for the epitaxial growth of 60 nm thick $(10\bar{1}0)$ $Co_{1-x(z)}Ru_{x(z)}$ compositionally modulated layers. The samples were covered by 10 nm thick protective SiO_x layers. The modulation of $x(z)$ was achieved through the variation of the Ru sputter rate during co-deposition of Co and Ru, with the average Ru concentration $\bar{x} = 0.235$ of the CoRu layer being 1.2 times that of the underlying $Cr_{1-0.83\bar{x}}Ru_{0.83\bar{x}}$ layer, the ideal ratio for the epitaxial growth [46]. The $Co_{1-x(z)}Ru_{x(z)}$ modulation scheme is depicted in Fig. 1(b). The Ru concentration varies periodically from $x = 0.26$ to $x = 0.21$ with a symmetric triangular waveform [40]. The defining characteristic of the samples is the modulation period λ between two consecutive minima in $x(z)$. For this work, we consider three systems with nominal $\lambda = 60$ nm, 20 nm, and 10 nm, as well as uniform $x = 0.21$, $x = 0.235$, and $x = 0.26$ reference samples grown using an identical underlayer sequence, with all magnetic CoRu films being 60 nm thick. For the remainder of the work, we will refer

to the experimental graded structure by their characteristic parameter λ (in units of nm), which corresponds to the nominal modulation period of each specific concentration profile. Analogously, we will later refer to the simulated systems featuring the corresponding exchange coupling strength profile characteristics by λ* (in units of atomic planes, *z*).

A complete structural analysis verifies that our samples have excellent crystallographic quality, with in-plane c-axis orientation over the entire composition and modulation range. Fig. 1(c) shows the Cu K_α x-ray diffraction measurements in the angular range $35° \leq 2\theta \leq 95°$. All scans exhibit only Si (220), Ag (220), Cr (211), CrRu (211), CoRu $(10\bar{1}0)$ and $(20\bar{2}0)$ crystal plane diffraction signals, demonstrating excellent crystallographic order. Figure 1(d) shows the XRD peaks for the $Co_{1-x(z)}Ru_{x(z)}$ $(10\bar{1}0)$ layers, normalized to the Ag (220) peak intensity of each individual sample. To allow for a side-by-side visual comparison, the individual peaks are shifted with respect to each other along the abscissa. As one can see from the data, the different $Co_{1-x(z)}Ru_{x(z)}$ $(10\bar{1}0)$ peaks are all very similar in their height and width, verifying the robustness of our fabrication process [46,48]. This also permits us to exclude the possibility that significant changes in magnetocaloric properties of the graded systems could be associated with a variable structural quality of the magnetic layers, but instead we can connect such changes with the different compositional modulation schemes. Figure 1(e) show exemplary XRD φ-scans for the λ = 20 nm sample, whose intensity has been normalized to the maximum value in each corresponding measurement. All φ-scans show two well-defined diffraction peaks that are 180° apart, which confirms the intended in-plane alignment associated with epitaxial growth [45,46]. Moreover, the overall narrow peak widths indicate excellent crystalline alignment. Therefore, the structural analysis verifies the high crystallographic quality of our $Co_{1-x(z)}Ru_{x(z)}$ graded films with the intended in-plane c-axis orientation that is the EA of magnetization for such alloys.

4. Magnetic characterization

For the purpose of verifying whether our samples exhibit the expected uniaxial magnetocrystalline anisotropy, we measured the RT sample magnetization as a function of a decreasing field strength 0.6 T $\geq \mu_0 H \geq$ 0.0 T and the angle ω between the c-axis and the applied field direction [46-48]. The experimental results are displayed for two exemplary samples, namely the homogenous $x = 0.235$ in Fig. 2(a) and the graded λ = 20 nm sample in Fig. 2(b). The color code represents the normalized magnetization data to the RT saturation magnetization M_S along the magnetic field axis. Both measurements in Fig. 2(a) and 2(b) show the prototypical behavior of a uniaxial ferromagnet with the EA parallel to the c-axis (ω = 0°,180°), and the hard axis perpendicular to it (ω = 90°,270°). For a quantitative analysis, we have performed least-squares fits of the magnetometry data to the energy expression of a simple macrospin model [46-49], and found excellent agreement for the entire set of samples, as exemplary shown in Figs. 2(c) - 2(d), with R^2 values better than 0.975. These observations

are reproduced in all the samples, confirming that they exhibit an in-plane uniaxial anisotropy behavior with the magnetization vector being homogenous within each plane and collinear everywhere. From our data analysis, we have extracted the magnetic anisotropy field H_k as well as the saturation magnetization M_S as fit parameters. As expected, M_S decreases upon increasing the Ru content x for the uniform $Co_{1-x}Ru_x$ samples [45,46], shown in Fig. 2(e). We also find that the modulated $Co_{1-x(z)}Ru_{x(z)}$ systems exhibit M_S values that are fairly constant and very similar to the homogenous sample of the same average composition. Figure 2(f) shows the best fit H_k parameters, indicating that the anisotropy field values of all samples are quite similar, as already reported for related exchange graded $Co_{1-x(z)}Cr_{x(z)}$ samples with similar J profiles [47,48].

Our further magnetometry investigations focused on characterizing the global T_C values in terms of the intrinsic defining characteristics of the compositional profiles. As such, the global T_C values were estimated using the Kuz'min method [50]. Fig. 2(g) shows the best fit T_C parameters for the uniform $Co_{1-x}Ru_x$ reference samples, whose values decrease in a linear fashion with x as expected and consistently with Refs. [46] and [47]. Fig. 2(h) shows the λ-dependency of T_C for the graded samples. As such, it is seen that T_C also decreases linearly with decreasing λ, even though the average Ru concentration in the graded $Co_{1-x(z)}Ru_{x(z)}$ samples remains the same, with the samples λ = 60 and 20 nm exhibiting T_C values significantly above the T_C of the average composition alloy. Therefore, we can assert that the T_C of the samples can not only be tailored by tuning the Ru concentration, but also by precisely controlling the gradient values of the pre-defined J distributions along z, consistent with numerical predictions discussed in Ref. [43].

5. Magnetocaloric properties in exchanged graded ferromagnets

The equations presented in this section were used to estimate the MCE properties for both experimental and simulated datasets. Formally, the magnetic entropy change (ΔS_m) can be expressed as using the following Maxwell relation [51],

$$\Delta S_m = \int_0^{H_f} \left(\frac{\partial M}{\partial T}\right)_T dH \,, \tag{1}$$

where H_f is the upper limit of the applied magnetic field intensity. Nonetheless, in the case of a discrete field, ΔS_m can be approximated by [52]

$$\Delta S_m(\Delta T) = \left(\frac{1}{\Delta T}\right)\left[\int_0^{H_f} M(T_2, H)dH - \int_0^{H_f} M(T_1, H)dH\right], \tag{2}$$

where $\Delta T = (T_2 + T_1) / 2$, with $T_2 > T_1$. To compute ΔS_m employing Eq. (2), it is necessary to measure/compute the magnetization as a function of the applied magnetic field at small discrete steps, for several isothermal processes [52,53].

As such, we performed M(H) measurements at several constant temperatures with decreasing field of 0.7 T ≥ μ_0H ≥ 0.0 T along the EA, which are displayed in Fig. 3 as lines for homogenous $Co_{1-x}Ru_x$ samples with $x = 0.26$ (a), 0.235 (b), and 0.21 (c) and for graded $Co_{1-x(z)}Ru_{x(z)}$ samples with different profiles λ = 60 (d), 20 (e), and 10 nm (f). The homogeneous CoRu samples exhibit qualitatively the same field- and temperature-dependence, showing that as the field is increased, there is a smearing of the magnetization onset, which is very typical of SOPT materials [1,18]. Even though the graded samples exhibit a similar smearing of the magnetization behavior upon increasing the applied magnetic field, the temperature range that is affected by the phase transition is much broader and smoother. In particular, for the λ = 60 nm sample the magnetization changes almost linearly with temperature (which is more visible from the low magnetic field region), whereas for larger λ, the overall shape of the M(H,T) curves tends towards that of the x = 0.235 reference sample, as can be seen upon close inspection of the data in Fig. 3.

Fig. 4 shows the determined temperature-dependent ΔS_m values at the largest applied field of μ_0H = 0.7 T for the three uniform $Co_{1-x}Ru_x$ reference samples with $x = 0.26$ (a), 0.235 (b), and 0.21 (c) and graded $Co_{1-x(z)}Ru_{x(z)}$ samples with different exchange strength profile modulations λ = 60 nm (d), λ = 20 nm (e), and λ = 10 nm (f). The resulting temperature dependent ΔS_m curves show the expected standard behavior of magnetic refrigerants, exhibiting a global maximum around each global T_C. Similar characteristics are found in the graded structure with the smallest λ, even though a magnetization and an exchange strength profiles are both present in this sample, suggesting that such system, close to its T_C, is magnetically strongly correlated throughout its thickness just as the uniform alloy systems. The effect of nanoscale J design becomes increasingly significant upon increasing λ [Fig. 4(d) and 4(e)], with the ΔS_m curves being significantly wider, especially for the sample with the largest λ = 60 nm. This is further highlighted by the yellow regions in each plot that represent the temperature range that is covered by the absolute difference in two selected reference temperatures (ΔT_r[1]), which serves as an estimation for the temperature operating range for magnetocaloric operation. Such increased ΔT_r for the graded structures is very promising since the ideal SOPT material for Ericsson-type magnetic refrigerators should exhibit a nearly constant ΔS_m value in a wide temperature range. In addition, the ΔS_m peak values (ΔS_m^{pk}) for the graded samples are found to be smaller than those of the homogeneous ones, since due to the predominantly local nature of the PM-FM phase transition [39,40,45,47,49] the overall change in the net magnetization of the whole structure close to T_C is smaller than in a uniform sample.

[1] $\Delta T_r = T_{r2} - T_{r1}$ defines the temperature range in which the ΔS_m curves exceeds 80% of its peak value (ΔS_m^{pk}) below (T_{r1}) and above (T_{r2}) T_C. The ΔS_m (T_{r1}) and ΔS_m (T_{r2}) are marked by red points in Fig. 4 (experiments) and Fig. 6 (simulations).

In order to characterize the magnetocaloric response of our materials regarding its intrinsic magnetic exchange distribution, the relative cooling power was computed as the area under the ΔS_m curves at the maximum applied magnetic field $\mu_0 H = 0.7$ T, using the reference temperatures below (T_{r1}) and above (T_{r2}) T_C as the integration limits[2], as follows

$$\mathrm{RCP}^* = \int_{T_{r1}}^{T_{r2}} \Delta S_m \, dT \, , \tag{3}$$

We present in Table 1 the experimentally obtained RCP* values for the experimental uniform and graded samples. The homogenous CoRu alloys exhibit an almost invariant RCP*, whereas for the graded samples there is a significant and important RCP* increase for the $\lambda = 60$ nm sample, followed by a monotonic decrease upon decreasing λ, with the RCP* values converging to the ones of the uniform alloys. Therefore, our experimental results show that it is possible to expand the range of accessible RCP values by ≈ 46% for $\lambda = 60$ nm, consisting in a truly remarkable performance gains, which could furthermore be optimized to fulfil operational needs by the deterministic control of the J modulation period λ.

6. Monte Carlo simulations results

To further validate the experimental observations of the previous sections, we performed MC simulations of the temperature- and field-dependent magnetization for each specific gradient sample explored in this work, following the numerical approach reported in Ref. [43]. Specifically, we considered an effective depth-dependent triangular wave exchange coupling profile, with the intralayer exchange strength J_z between a spin and its nearest neighbors in the same layer given by:

$$J_z = \left| \frac{2(J_{max} - J_{min})}{\pi} \arcsin\left(\sin\left(\frac{\pi}{\lambda} z\right)\right) \right| + J_{min} \, , \tag{4}$$

where λ is the modulation period in units of atomic layers (z), with $0 \leq z \leq 60$, thus, mimicking the experimental samples shown in Fig. 1(b). For simplicity we choose $J_{max} = 1.0$ so that J_{min} corresponds to the ratio of the Curie temperature of two uniform reference samples T_C ($Co_{0.74}Ru_{0.26}$) / T_C ($Co_{0.79}Ru_{0.21}$) [43]. The interlayer exchange strength $J_{z(z+1)}$ is defined as the arithmetic average $J_{z(z+1)} = (J_z + J_{z+1})/2$. The magnetic properties were simulated using a Heisenberg Hamiltonian that is a superposition of layer-wise terms, considering only nearest neighbors exchange interactions [43] and the interaction of the spins with an applied magnetic field as follows:

[2]Generally, the integration limits in Eq. (3) correspond to the temperatures at (FWHM) of the ΔS_m curves [51]. However, we have selected this sort of arbitrary threshold, because in some cases, we could not access the FWHM values of the corresponding curves due to experimental restrictions associated with accessible temperature range in our experiments.

$$\mathcal{H} = -\sum_{z=0}^{t}\left(\sum_{\langle i,j\rangle} J_z(\boldsymbol{S}_i\,.\,\boldsymbol{S}_j) + \sum_{\langle i,k\rangle} J_{z(z+1)}(\boldsymbol{S}_i\,.\,\boldsymbol{S}_k)\right) - H\sum_i \boldsymbol{S}_i\,.\,\widehat{\boldsymbol{k}}\,, \tag{5}$$

where t is the total thickness of the sample in units of atomic layers (z), so that $0 \leq z \leq t$. As described in Section 2, we have considered a fixed system size of $L = 20$ and $t = 60$, with PBC imposed in the x-y plane, and FBC imposed along the z-axis for all simulated samples explored in this work. Moreover, $\boldsymbol{S}_i$, $\boldsymbol{S}_j$, and $\boldsymbol{S}_k$ are the spins of the magnetic sites labeled i, j, k, where these labels denote that the summations are taken to account for the interactions a of spin i with its j and k nearest neighbours in the same and adjacent atomic plane, considering $|\boldsymbol{S}_i| = |\boldsymbol{S}_j| = |\boldsymbol{S}_k| = 1$. It is important to note that the first and second terms in Eq. (5) correspond to the intra- and inter-layer exchange interaction respectively, whereas the third term corresponds to the Zeeman energy term to describe the interaction of the magnetic moments with an externally applied magnetic field. In this study, we assume the magnetic field pointing in the z-direction, perpendicular to the plane of each layer, therefore, $\widehat{\boldsymbol{k}}$ represents the canonical vector in the z–direction, and H is the magnetic field intensity. We have neglected for simplicity anisotropy and magnetostatic energy terms in our MC simulations, since our magnetometry investigation of MCE was solely performed along the EA of our epitaxial samples, along which the systems exhibit magnetization states that are dominated by exchange interactions and simple magnetization reversal behavior.

Simulations of the M(T) behavior were performed with temperatures ranging from $k_B\mathrm{T}/J_{max} = 4.5$ down to $k_B\mathrm{T}/J_{max} = 0.01$, for three uniform reference samples with J_{max}, J_{min}, and J_{avg} (mimicking $x = 0.21$, 0.26, and 0.235 samples respectively, with J_{avg} being the average between J_{max} and J_{min}) and for four modulated graded systems with the characteristic modulation period of the simulated samples, namely $\lambda^* = 60$, 20, 10, and 4. Fig. 5 displays the measured global T_C (red squares), compared on a relative scale with the simulated global T_C values (blue circles). As expected, the T_C of the simulated uniform samples decreases almost linearly with J [40,46], while the T_C of the modulated structures exhibits a monotonic decrease upon decreasing λ^*, converging to the value of a uniform sample with average J. Also, Fig. 5 shows that albeit there is a clearly distinguishable λ dependency of T_C, this dependency is much weaker than the J-dependence itself, which turns out to be in excellent agreement with our experimental observations presented in Figs. 2(g) and (h). Therefore, the overall λ dependency of T_C can be very well reproduced by our computational model for the here explored uniform and exchange modulated samples, which in turn verifies that our model successfully reproduces all key T_C features despite its inherent simplifying assumptions [43].

Based on the results in Fig. 5, it is important to define the quantity $J_{eff} = \mathrm{T_C}/T_C^b$ (whose values are listed in Table 1) to properly model the relative influence of the applied magnetic field on the magnetic properties at a given temperature, with T_C^b being the T_C of a 3-dimensional homogeneous

system with J_{max}. In the case of the homogeneous samples, J_{eff} takes trivial values considering the frame of our simulated systems, whereas for the graded samples it reduces monotonically upon reducing λ*, as it is intended to account for the yet effectively ferromagnetically ordered region of the graded sample that still contributes to T_C [43]. Fig. 6 shows the ΔS_m dependence on the normalized temperature k_BT/J_{eff} for the largest applied field (H/J_{eff} = 1.0) for the three simulated uniform reference samples with J_{min} (a), J_{avg} (b), J_{max} (c), and for three exchange modulated samples featuring symmetric triangular wave profiles with (d) λ* = 60, (e) λ* = 20, (f) λ* = 10 in units of the number of layers, z. As expected, the three uniform samples show ΔS_m^{pk} values that are the same within the error, regardless of J, since all these systems are fundamentally equal. Therefore, their magnetocaloric response exhibits an identical behavior, but shifted in temperature according to the respective value of J. In contrast to these uniform samples, the graded structures exhibit ΔS_m curves that have a broader temperature width compared to the uniform structures, a broadening that reduces upon decreasing the modulation wavelength, which is in excellent agreement with our experimental findings. Moreover, Fig. 6 shows that an interesting trade-off emerges between ΔS_m and ΔT_r in graded systems, which can be precisely tuned and may overcome operational needs in magnetic refrigeration systems. Also, it is observed that the ΔT_r increases by a factor of about 2 for the λ* = 60 sample without compromising the ΔS_m^{pk} values. As such, it is observed that albeit the ΔS_m^{pk} values are only minorly reduced upon inducing compositional (exchange) gradients on both experimental and simulated samples, the temperature range in which ΔS_m exhibits values larger than 80% of ΔS_m^{pk} is significantly wider if compared to that of the uniform reference samples, which furthermore represents a truly remarkable result towards improving the magnetocaloric response of magnetic materials over an ever-wider and nanoscale-controlled temperature operation range.

As already mentioned in the introduction, previous studies concluded that the ideal material for Ericsson-type magnetic refrigerators should exhibit a nearly constant value of ΔS_m in the temperature range of the operation of the thermodynamic cycle [18]. Therefore, by considering the previous evidence and discussion presented in this work, we computed the RCP* for the simulated uniform and graded structures at the largest applied magnetic field (H/J_{eff} = 1.0) following Eq. (3), whose results are listed in Table 1. As expected, the simulated uniform samples exhibit an almost invariant RCP*, whereas the graded samples show a significant increase of ≈ 160% for the λ* = 60 sample when compared to the uniform systems, which is followed by a monotonic decrease of RCP* upon decreasing λ, even extending to the simulated limit case sample of λ* = 4 that behaves predominantly as a uniform system. As such, when considering the excellent qualitative agreement between experiments and simulations, we are demonstrating that nanoscale designed graded materials should be considered as an optimal material platform to fulfill MCE operational requirements, since it sets a starting point for

exploring the magnetocaloric properties from both theoretical and experimental approaches, while still being interesting from a fundamental perspective to understand magnetic phenomena at the nanoscale.

7. Conclusions

In this work, we demonstrated a proof-of-concept approach to achieve nanoscale control of the operating temperature range for magnetocaloric applications that results in substantial performance improvements, consisting of graded epitaxial $Co_{1-x(z)}Ru_{x(z)}$ thin films that are characterized by an exchange coupling modulation wavelength λ. We explored the field-dependency of the magnetization for selected sample structures for several isothermal processes to assess the magnetocaloric properties. We have observed that the relevant phase transition region for properly designed graded samples was significantly broader, especially for those exhibiting sufficiently large λ. Particularly, it was found that the magnetic entropy change ΔS_m curves exhibit a well-defined and precisely tunable behavior, whose width can be increased by a factor of about 2 in graded structures if compared to homogenous alloy systems having the same average composition, a fact that leads to significant performance gains in terms of the RCP.

Moreover, the qualitative agreement between MC simulations and experiments is excellent especially if we consider that the computations were carried out considering only exchange interactions, so that we can assert the dominance of this term on defining the temperature and field dependency of the samples explored in this work. Indeed, our simulations show the feasibility to estimate to a high degree of confidence the operating temperature range for magnetocaloric applications, and they can be straightforwardly extended to a sample featuring an arbitrary exchange profile, which can be material engineered to fulfill operational needs.

Despite our samples are rather specialized materials and only representative of one class of alloys, the results are generally applicable to exchange strength graded materials. Our findings clearly show a pathway towards the optimization of magnetocaloric behavior by means of nanoscale material design, which could in principle be implemented as an improved materials engineering approach even for mass produced compounds, once upscaling strategies will be developed assuring other physical properties such as mechanical, electrical, and corrosion resistance characteristics [18].

ACKNOWLEDGMENTS

J. S. Salcedo-Gallo acknowledges financial support by MINCIENCIAS under the program Jóvenes Investigadores e Innovadores 2018 (Grant No. 812) and financial support by Universidad Nacional de Colombia under the program Convocatoria Nacional para la Movilidad Internacional 2019-2021 (Grant No. 10877). Work at nanoGUNE acknowledges financial support by the Spanish Ministry of Science and Innovation under the Maria de Maeztu Units of Excellence Program (MDM-2016-0618) and Project

No. RTI2018-094881-B-100 (MICINN/Feder). Mikel Quintana acknowledges financial support by predoctoral fellowship No. PRE2019-088428.

Figure Captions

Figure 1. (a) Schematic of the growth sequence used here; (b) shows the three corresponding Ru content depth-dependent profiles that have been explored; (c) XRD θ–2θ measurements for the three uniform $Co_{1-x}Ru_x$ samples with different Ru concentrations x and for the three graded $Co_{1-x(z)}Ru_{x(z)}$ structures with different Ru modulation λ. Each scan has been normalized to the intensity of its Ag (220) peak and shifted along the abscissa for a side-by-side visual comparison; (d) displays the CoRu $(10\bar{1}0)$ peaks for different Ru concentrations and profiles (x and λ values are indicated), normalized to the corresponding Ag (220) peak intensity of the same sample. For clarity, the individual peaks are shifted with respect to each other along the x-axis. (e) Representative XRD φ-scans of the 2θ poles of Si {400}, Ag {200}, Cr {110}, and CoRu $\{10\bar{1}1\}$ for the λ = 20 sample.

Figure 2. (a) - (b) In-plane angular dependence of the magnetization measured from saturation to remanence by VSM at room temperature (RT) for homogenous $Co_{1-x}Ru_x$ samples with x = 0.235 and for the graded $Co_{1-x(z)}Ru_{x(z)}$ sample with λ = 20. The data are normalized to the RT saturation magnetization M_S and are displayed as color-coded maps as a function of the applied field angle ω with respect to the easy axis and the field strength H. (c) - (d) show the corresponding least-squares fits of the data based upon the minimization of the total energy as defined in [46,47]. The resulting RT saturation magnetization M_S and anisotropy field H_k of all the samples are displayed in (e) and (f) respectively. (g) - (h) Experimentally determined Curie temperatures (T_C) for homogenous (g) and graded (h) samples. The green line in (h) marks the T_C for the homogenous sample with x = 0.235 while the light green rectangle indicates the error level.

Figure 3. Temperature dependence of the normalized magnetization $M_0 = M/M_S(T/T_C = 0.8)$, which were measured in the presence of 0.7 T ≥ μ_0H ≥ 0.0 T decreasing field for homogenous $Co_{1-x}Ru_x$ samples with x = 0.26 (a), 0.235 (b), and 0.21 (c) and graded $Co_{1-x(z)}Ru_{x(z)}$ samples with different profiles λ = 60 nm (d), λ = 20 nm (e), and λ = 10 nm (f). The 2-dim colour coded maps of each graph are the results of data interpolation, which was then used to calculate the ΔS_m data of Fig. 4. The color bar in (a) applies to (a) – (f).

Figure 4. Temperature dependence of magnetic entropy change $-\Delta S_m$ for the three homogenous samples with x = 0.26 (a), x = 0.235 (b), x = 0.21 (c), and for the three graded samples with λ = 60 nm (d), λ = 20 nm (e), λ = 10 nm (f). The $-\Delta S_m$ has been calculated for magnetic fields changes 0.7 T ≥ μ_0H ≥ 0.0 T . The red dots in each graph indicate the $-\Delta S_m^{pk} \times 0.8$ threshold for the evaluation of the ΔT_r, whose area is highlighted in yellow.

Figure 5. "Global" T_C for simulated (blue circles) and experimental (red squares) samples plotted on a relative scale. The bottom-right (red) axes refer to the experimental data, whereas the top-left (blue) axes refer to the simulated data points.

Figure 6. Temperature dependence of the simulated magnetic entropy change $-\Delta S_m$ for the three homogenous structures J_{min}, J_{avg}, and J_{max}, and for three systems featuring a gradient magnetic exchange profile as in Fig. 6, which were calculated for the largest magnetic field H/J_{eff} = 1.0. The red dots in each graph indicate the $-\Delta S_m^{pk}\times 0.8$ threshold points for the evaluation of σ.

Table 1. Relative cooling power (RCP)* calculated as RCP* $= \int_{Tr_1}^{Tr_2} \Delta S_m \, dT$ together with the J_{eff} values for the simulated homogeneous and graded structures.

	$x = 0.21$	$x = 0.235$	$x = 0.26$	$\lambda = 60$ nm	$\lambda = 20$ nm	$\lambda = 10$ nm	
*RCP** (J/Kg)	2.4	2.1	2.6	3.5	3.15	2.2	
	$J = 1$	$J = 0.75$	$J = 0.5$	$\lambda^* = 60$	$\lambda^* = 20$	$\lambda^* = 10$	$\lambda^* = 4$
J_{eff}	1	0.75	0.5	0.98	0.92	0.86	0.78
*RCP** (arb.u.)	0.069	0.065	0.067	0.18	0.16	0.12	0.080

Figure 1

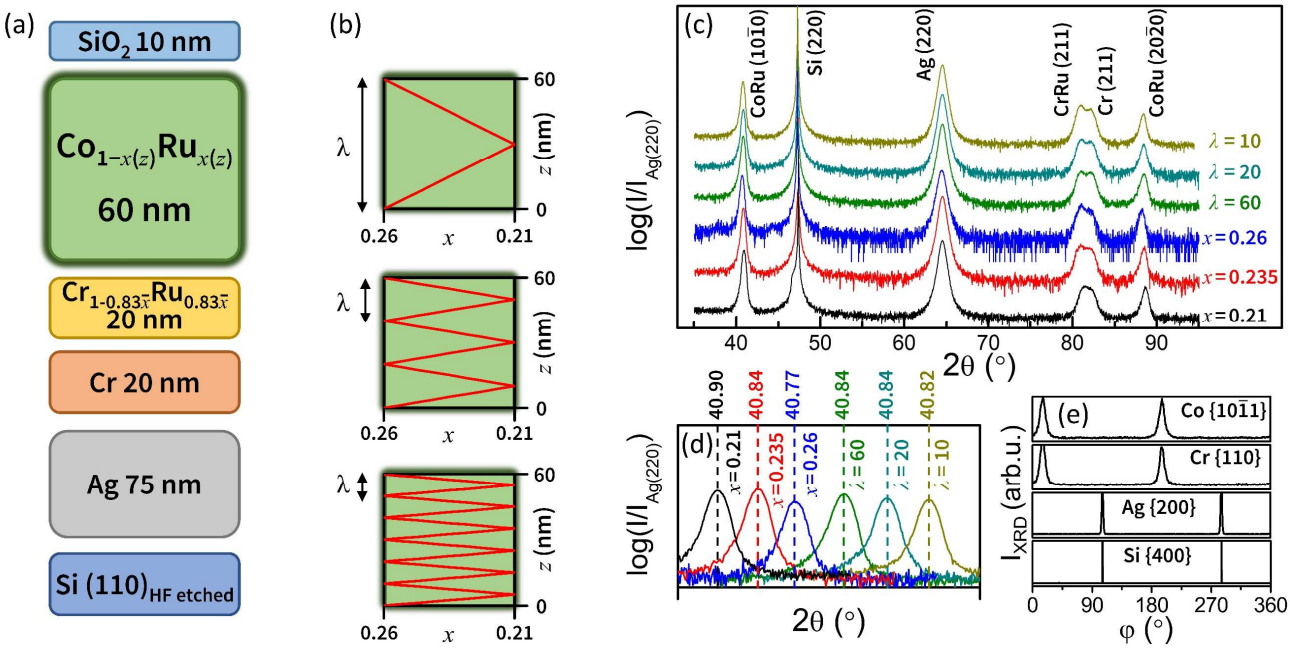
(a)
SiO2 10 nm
Co1−x(z)Rux(z)
60 nm
Cr1-0.83x̄Ru0.83x̄
20 nm
Cr 20 nm
Ag 75 nm
Si (110)HF etched
(b)
λ
60
z (nm)
0
0.26
x
0.21
(c)
CoRu (10$\bar{1}$0)
Si (220)
Ag (220)
CrRu (211)
Cr (211)
CoRu (20$\bar{2}$0)
λ = 10
λ = 20
λ = 60
x = 0.26
x = 0.235
x = 0.21
log(I/IAg(220))
40
50
60
70
80
90
2θ (°)
(d)
40.90
40.84
40.77
40.84
40.84
40.82
x = 0.21
x = 0.235
x = 0.26
λ = 60
λ = 20
λ = 10
2θ (°)
(e)
Co {10$\bar{1}$1}
Cr {110}
Ag {200}
Si {400}
IXRD (arb.u.)
0
90
180
270
360
φ (°)

Figure 2

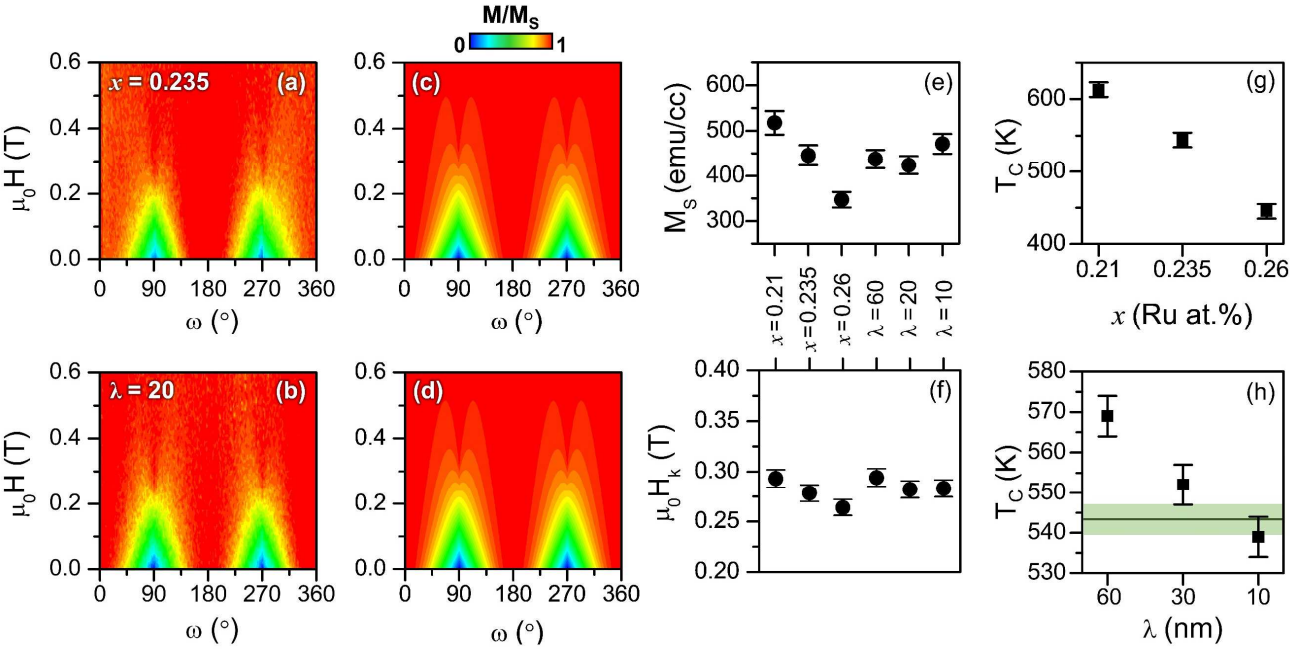
M/M$_S$
0
1
x = 0.235
(a)
(c)
λ = 20
(b)
(d)
μ_0H (T)
ω (°)
0.0
0.2
0.4
0.6
0
90
180
270
360
(e)
M_S (emu/cc)
300
400
500
600
x=0.21
x=0.235
x=0.26
λ=60
λ=20
λ=10
(f)
$\mu_0 H_k$ (T)
0.20
0.25
0.30
0.35
0.40
(g)
T_C (K)
400
500
600
0.21
0.235
0.26
x (Ru at.%)
(h)
530
540
550
560
570
580
60
30
10
λ (nm)

Figure 3

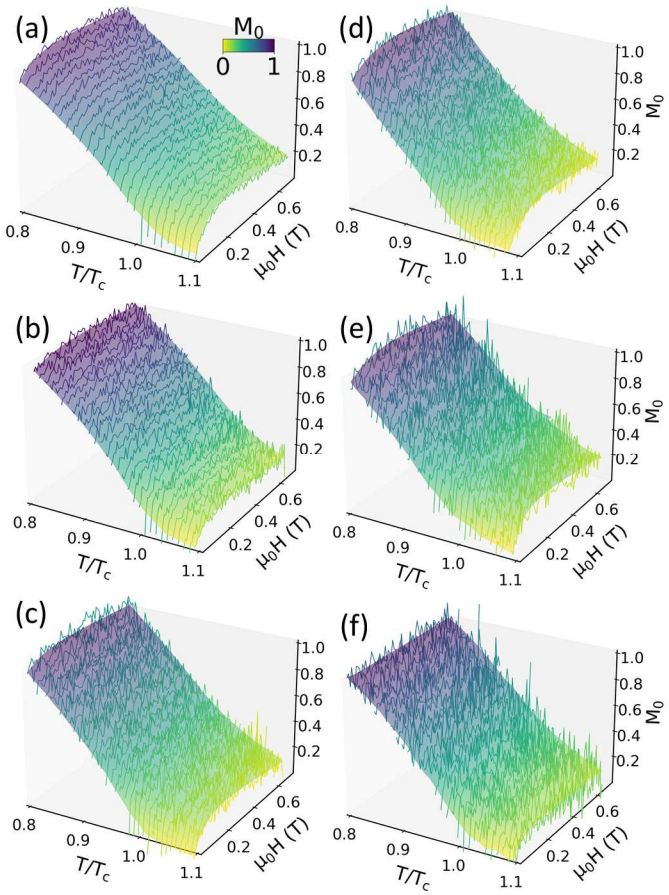

Figure 4

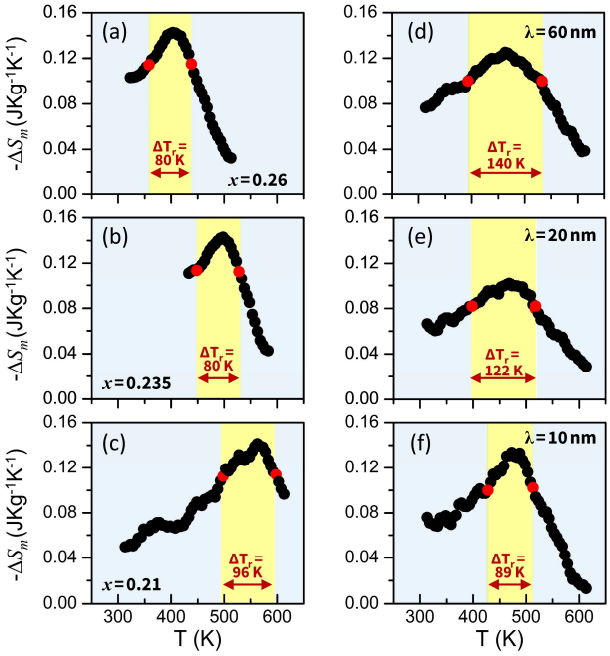
(a)
x=0.26
ΔT_r = 80 K
(b)
x=0.235
ΔT_r = 80 K
(c)
x=0.21
ΔT_r = 96 K
(d)
λ=60 nm
ΔT_r = 140 K
(e)
λ=20 nm
ΔT_r = 122 K
(f)
λ=10 nm
ΔT_r = 89 K
-ΔS_m (JKg^-1K^-1)
T (K)
0.00
0.04
0.08
0.12
0.16
300
400
500
600

Figure 5

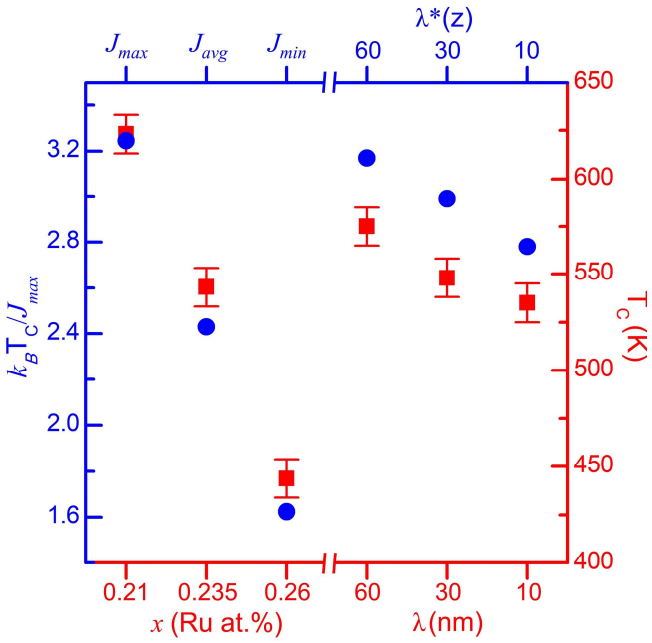
λ*(z)
J_{max}
J_{avg}
J_{min}
60
30
10
650
600
550
500
450
400
3.2
2.8
2.4
2.0
1.6
$k_B T_C / J_{max}$
T_C (K)
0.21
0.235
0.26
60
30
10
x (Ru at.%)
λ (nm)

Figure 6

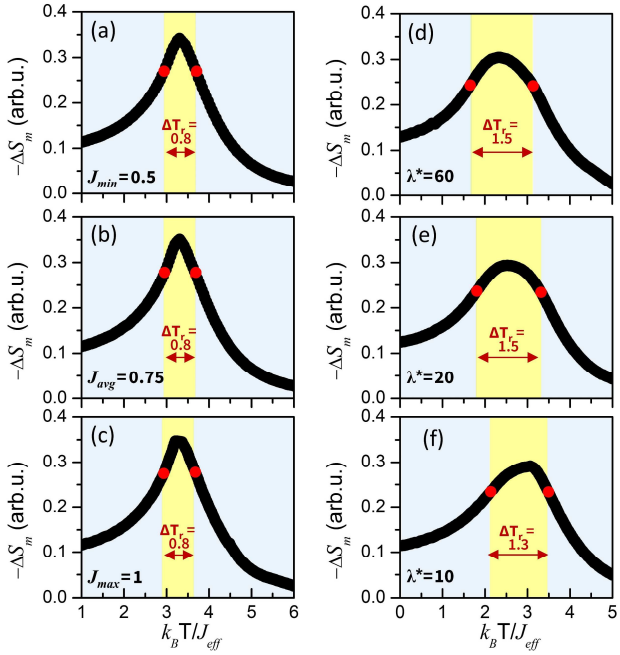
(a)
(b)
(c)
(d)
(e)
(f)
$-\Delta S_m$ (arb.u.)
$k_B T/J_{eff}$
J_{min}=0.5
J_{avg}=0.75
J_{max}=1
λ*=60
λ*=20
λ*=10
ΔT_r = 0.8
ΔT_r = 1.5
ΔT_r = 1.3

References

[1] P Weiss and A Piccard**,** J. Phys. Theor. Appl. **7**, 103-109 (1917)

[2] A. Smith, Eur. Phys. J. H **38**, 507–517 (2013).

[3] J. Romero Gómez, R. Ferreiro Garcia, A. De Miguel Catoira, and M. Romero Gómez, Renew. Sustain. Energy Rev. **17**, 74 (2013).

[4] W. F. Giauque and D. P. MacDougall, *Phys. Rev.* **43**, 768 (1933).

[5] G. V. Brown, J. Appl. Phys. **47**, 3673 (1976).

[6] A. Berger, A. W. Pang, and H. Hopster, Phys. Rev. B **52**, 1078 (1995).

[7] K. A. Gschneidner Jr. and V. K. Pecharsky, Int. J. Refrig. **31**, 945 (2008).

[8] O. Tegus, E. Brück, K. H. J. Buschow, and F. R. de Boer, Nature **415**, 150 (2002).

[9] A. Fujita, S. Fujieda, Y. Hasegawa, and K. Fukamichi, Phys. Rev. B **67** 104416 (2003).

[10] K. A. Gschneidner Jr, V. K. Pecharsky and A. O. Tsokol, Rep. Prog. Phys. **68**, 1479 (2005).

[11] T. Krenke, E. Duman, M. Acet, E. F. Wassermann, X. Moya, L. Manosa, and A. Planes, Nat. Mater. **4**, 450 (2005).

[12] E. Brück, O. Tegus, D. T. Cam Thanh, T. T. Nguyen, and K. H. J. Buschow, Int. J. Refrig. **31**, 763 (2008).

[13] O. Gutfleisch, M. A. Willard, E. Bruck, C. H. Chen, S. G. Sankar, and J.Ping Liu, Adv. Mater. **23**, 821 (2011).

[14] J. Liu, T. Gottschall, K. P. Skokov, J. D. Moore, and O. Gutfleisch, Nature Mater. **11**, 620 (2012).

[15] V. K. Pecharsky and K. A. Gschneidner Jr., Phys. Rev. Lett. **78**, 4494 (1997).

[16] V. I. Zverev, A. M. Tishin, and M. D. Kuz'min, J. Appl. Phys. **107**, 043907 (2010).

[17] A. M. Tishin, J. Magn. Magn. Mater. **316**, 351 (2007).

[18] V. Franco, J. S. Blázquez, B. Ingale, and A. Conde, Annu. Rev. Mater. Res. **42**, 305 (2012).

[19] A. Smaïli and R. Chahine, J. Appl. Phys. **81**, 824 (1997).

[20] R. Caballero-Flores, V. Franco, A. Conde, K. E. Knipling, and M. A. Willard, Appl. Phys. Lett. **98**, 102505 (2011).

[21] B. Chevalier, J.-L. Bobet, J. Sánchez Marcos, J. Rodriguez Fernandez, andJ. C. Gómez Sal, Appl. Phys. A: Mater. Sci. Process. **80**, 601 (2005).

[22] H. Ucar, J. J. Ipus, V. Franco, M. E. McHenry, and D. E. Laughlin, JOM **64**, 782–788 (2012).

[23] W. H. Wang, Prog. Mater. Sci. **52**, 540 (2007).

[24] Q. Zhang, J. Du, Y. B. Li, N. K. Sun, W. B. Cui, D. Li, and Z. D. Zhang, J. Appl. Phys. **101**, 123911 (2007).

[25] D. Wang, K. Peng, B. Gu, Z. Han, S. Tang, W. Qin, and Y. Du, J. Alloys Compd. **358**, 312 (2003).
[26] P. Gorria, J. L. Sánchez Llamazares, P. Álvarez, M. J. Pérez, J. Sánchez Marcos, and J. A. Blanco, J. Phys. D: Appl. Phys. **41**, 192003 (2008).
[27] J. H. Belo, A. L. Pires, J. P. Araújo, and A. M. Pereira, J. Mater. Res. **34**, 134 (2019).
[28] X. Moya, L. E. Hueso, F. Maccherozzi, A. I. Tovstolytkin, D. I. Podyalovskii, C. Ducati, L. C. Phillips, M. Ghidini, O. Hovorka, A. Berger, M. E. Vickers, E. Defay, S. S. Dhesi, and N. D. Mathur, Nature Mat. **12**, 52-58 (2013).
[29] A. L. L. Sharma, P. A. Sharma, S. K. McCall, S. B. Kim, and S. W. Cheong, Appl. Phys. Lett. **95**, 092506 (2009).
[30] A. Biswas, T. Samanta, S. Banerjee, and I. Das, Appl. Phys. Lett. **92**, 012502 (2008).
[31] Y. Shao, J. Zhang, J. K. L. Lai, and C. H. Shek, J. Appl. Phys. **80**, 76 (1996).
[32] F. Shir, L. Yanik, L. H. Bennett, E. Della Torre, and R. D. Shull, J. Appl. Phys. **93**, 8295 (2003).
[33] C. E. Reid, J. A. Barclay, J. L. Hall, and S. Sarangi, J. Alloys Compd. **207–208**, 366-371 (1994).
[34] M. A. Richard, A. M. Rowe, and R. Chahine, J. Appl. Phys. **95**, 2146 (2004).
[35] C. W. Miller, D. D. Belyea, and B. J. Kirby, J. Vac. Sci. Technol. A **32**, 040802 (2014).
[36] C. W. Miller, D. V. Williams, N. S. Bingham, and H. Srikanth, J. Appl. Phys. **107**, 09A903 (2010).
[37] I. G. De Oliveira, P. J. Von Ranke, and E. P. Nóbrega, J. Magn. Magn. Mater. **261**, 112 (2003).
[38] A. Chaturvedi, S. Stefanoski, M.-H. Phan, G. S. Nolas, and H. Srikanth, Appl. Phys. Lett. **99**, 162513 (2011).
[39] B. J. Kirby, H. F. Belliveau, D. D. Belyea, P. A. Kienzle, A. J. Grutter, P. Riego, A. Berger, and C. W. Miller, Phys. Rev. Lett. **116**, 047203 (2016).
[40] B. J. Kirby, L. Fallarino, P. Riego, B. B. Maranville, C. W. Miller, and A. Berger, Phys. Rev. B **98**, 064404 (2018).
[41] C. Eyrich, A. Zamani, W. Huttema, M. Arora, D. Harrison, F. Rashidi, D. Broun, B. Heinrich, O. Mryasov, M. Ahlberg, O. Karis, P. E. Jönsson, M. From, X. Zhu, and E. Girt, Phys. Rev. B **90**, 235408 (2014).
[42] L. Li, O. Niehaus, M. Kersting,and R. Pöttgen, Appl. Phys. Lett. **104**, 092416 (2014).
[43] J. S. Salcedo-Gallo, L. Fallarino, J. D. Alzate-Cardona, E. Restrepo-Parra, and A. Berger, "Monte Carlo simulations of the thermodynamic behavior of exchange graded ferromagnets", accepted in Phys. Rev. B on the 6/03/2021.
[44] J. D. Alzate-Cardona, D. Sabogal-Suárez, R. F. L. Evans, and E. Restrepo-Parra, J. Phys. Condens. Matter **31**, 95802 (2019).
[45] W. Yang, D. N. Lambeth, and D. E. Laughlin, J. Appl. Phys. **87**, 6884 (2000).

[46] O. Idigoras, U. Palomares, A. K. Suszka, L. Fallarino, and A. Berger, Appl. Phys. Lett. **103**, 102410 (2013).

[47] L. Fallarino, B. J. Kirby, M. Pancaldi, P. Riego, A. L. Balk, C. W. Miller, P. Vavassori, and A. Berger, Phys. Rev. B **95**, 134445 (2017).

[48] L. Fallarino, P. Riego, B. Kirby, C. Miller, and A. Berger, Materials **11**, 251 (2018).

[49] P. Riego, L. Fallarino, C. Martínez-Oliver, and A. Berger, Phys. Rev. B **102**, 174436 (2020).

[50] M. D. Kuz'min, Phys. Rev. Lett. **94**, 107204 (2005).

[51] V. Franco, J. S. Blázquez, B. Ingale, and A. Conde, Annu. Rev. Mater. Res. **42**, 305 (2012).

[52] J. S. Salcedo-Gallo, D. F. Rodríguez-Patiño, J. D. Alzate-Cardona, H. Barco-Ríos, and E. Restrepo-Parra, Phys. Lett. Sect. A Gen. At. Solid State Phys. **382**, 2069-2074 (2018).

[53] J. D. Alzate-Cardona, J. S. Salcedo-Gallo, D. F. Rodríguez-Patiño, C. D. Acosta-Medina, and E. Restrepo-Parra, Sci. Rep. **9**, 5228 (2019).